

Programmable quantum simulation of anharmonic dynamics

Cameron McGarry,^{1,2,*} Teerawat Chalermputitarak,^{1,2} Kai Schwennicke,³ Frank Scuccimarra,¹
Maverick J. Millican,¹ Vassili G. Matsos,¹ Christophe H. Valahu,^{1,2} Prachi Nagpal,¹
Hon-Kwan Chan,¹ Henry L. Nourse,³ Ivan Kassal,^{3,2} and Ting Rei Tan^{1,2,†}

¹*School of Physics, University of Sydney, NSW 2006, Australia*

²*University of Sydney Nano Institute, University of Sydney, NSW 2006, Australia*

³*School of Chemistry, University of Sydney, NSW 2006, Australia*

Continuous-variable–discrete-variable (CV–DV) quantum simulators offer a natural route to simulating bosonic dynamics relevant to many branches of physics and chemistry. However, programmable simulation of arbitrary dynamics is an outstanding challenge. In particular, simulating anharmonic dynamics, which is ubiquitous across the physical sciences, is difficult due to the highly harmonic nature of oscillators used in CV–DV simulators. Here, we experimentally demonstrate programmable CV–DV quantum simulation of anharmonic dynamics in a range of double-well potentials, implemented in a trapped-ion system. We synthesise the time-evolution operators using a bosonic-quantum-signal-processing subroutine, which allows the potential to be tuned between experiments by controlling classical experimental parameters. We observe coherent dynamics in various double-well potentials, where a wavepacket tunnels through the potential barrier, and we suppress this effect by programmatically introducing asymmetry.

Quantum simulation is emerging as a powerful tool for efficiently capturing the dynamics of complex quantum systems that are intractable with classical approaches [1–9]. A promising quantum-simulation paradigm is the direct encoding of continuous-variable (CV) degrees of freedom of the simulated system into controllable oscillators [2, 10–12]. This paradigm can significantly reduce the required quantum resources compared to qubit-only simulations, because discretising CV information into qubits requires deep circuits on many qubits [10, 11, 13–18]. Quantum simulators employing CV systems as resources have been used to simulate chemical dynamics [16, 19–30] and high-energy physics [31–33]; there are also proposals to use them to study quantum field theories [11, 17, 34, 35], condensed matter physics [12, 17] and quantum chaos [36].

A central challenge in CV-based simulation is capturing anharmonic dynamics. Quantum simulators typically use high-quality harmonic CV degrees of freedom. Hence, simulating anharmonicity requires realising non-Gaussian operators, which typically rely on weak nonlinear interactions and are therefore challenging to implement. Nevertheless, the anharmonic regime is important in chemistry, because many molecular vibrations are anharmonic [37–44], as well as in quantum field theory [45] and quantum many-body systems [46–48].

Although simulations of anharmonic dynamics have been achieved, their programmability has been limited. Programmability is the ability to choose a target Hamiltonian by varying experimental parameters without modification of the underlying hardware. This would enable high-throughput quantum simulations without the need to build Hamiltonian-specific hardware.

Existing approaches to simulating anharmonic dynamics have been limited in several ways. For instance, simulations of anharmonicity with photonic systems are limited by weakly nonlinear optical elements [21, 30]. Tailored superconducting circuit quantum electrodynamics devices were used to simulate dissipative dynamics in anharmonic potentials [49], but the range of simulable dynamics is constrained by the device’s always-on dispersive qubit-oscillator interaction that limits coher-

ence and tunability. Similarly, trapped-ion devices allow implementing specific anharmonic dynamics through customised devices [50–53] or engineered light-atom couplings [54–56]. However, these devices lack an efficient compilation layer between target evolution operators and experimentally accessible gates, which limits the anharmonic potentials that can be simulated.

Bosonic quantum signal processing (BQSP) presents a route to programmable quantum simulation of anharmonic dynamics. BQSP operates on hybrid systems composed of both CV and discrete variable (DV) degrees of freedom, such as qubits. It uses CV–DV primitives—qubit-state-dependent displacements (SDD) and single-qubit rotations (SQR)—which are interleaved to realise a nonlinear transformation on the CV subsystem. While universal control of CV–DV simulators has long been established [54, 57–60], BQSP allows the construction of non-Gaussian operators in a systematic fashion with a well-defined circuit structure and error scaling by appropriately choosing amplitudes and phases for the primitive operations [61–68]. Furthermore, BQSP techniques can construct an operator that encodes the time evolution under a target Hamiltonian, enabling simulation of dynamics.

Here, we demonstrate a programmable quantum simulation of anharmonic dynamics. Specifically, we implement several double-well potentials (Fig. 1), which are of particular interest across physics [69, 70] and chemistry [71–78]. These potentials are implemented using the trigonometric-gate-implemented Fourier synthesis (TGIFS) scheme, which compiles the dynamics into a BQSP sequence of primitive SDD and SQR gates. Importantly, the potentials are fully programmable, as their defining parameters are entirely determined by parameters in the SDD and SQR gates. We perform the experiment using a single trapped ion, and implement the gates through light-atom interactions. We observe the wavepacket dynamics and quantum tunnelling through the potential barrier, which diminishes when we increase the asymmetry of the potential.

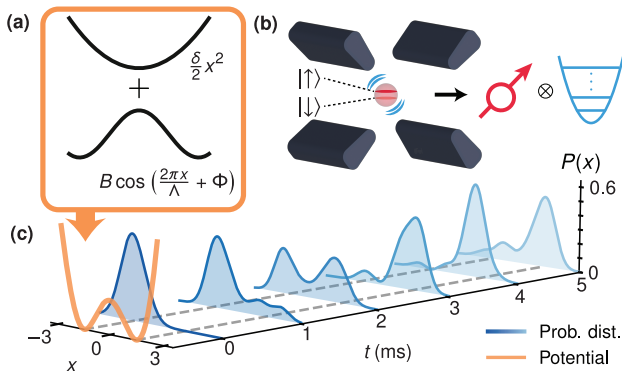


Figure 1. **Quantum simulation of dynamics in an anharmonic potential.** (a) A double-well potential is synthesised using a parabolic contribution and a cosine contribution from a trigonometric gate. (b) A trapped-ion quantum simulator, with the spin providing the qubit and the motion the oscillator. (c) Dynamics in a symmetric double well; a wavepacket initialised in one well tunnels through the barrier to the opposite well.

I. SIMULATING ANHARMONICITY

We simulate quantum dynamics in anharmonic potentials using TGIFS [66], which describes simulation of the Hamiltonian

$$H = \frac{\delta}{2}(x^2 + p^2) + V(x), \quad (1)$$

where δ is the frequency of the oscillator's harmonic component, $x = (a + a^\dagger)/\sqrt{2}$ and $p = -i(a - a^\dagger)/\sqrt{2}$ are the dimensionless position and momentum operators, respectively, and $V(x)$ is a time-independent anharmonic potential. In TGIFS, $V(x)$ is decomposed into a Fourier series whose terms are individually synthesised using a set of non-Gaussian operators. We consider the one-dimensional case (i.e., a single mode), but TGIFS can be straightforwardly extended to multiple modes, allowing one to simulate any potential that is a function of mutually commuting oscillator quadratures [66].

We simulate the dynamics generated by H in the interaction picture with respect to the harmonic term. In this picture, the dynamics is governed by

$$H_I(t) = U_0^\dagger(t) H U_0(t), \quad (2)$$

$$= V(x_I(t)), \quad (3)$$

where $U_0(t) = \exp(-i\frac{\delta}{2}(x^2 + p^2)t)$ and $x_I(t) = (ae^{-i\delta t} + a^\dagger e^{i\delta t})/\sqrt{2}$ is the time-dependent position operator. The goal is to simulate the unitary evolution generated by $H_I(t)$ from t_0 to T ,

$$U(t_0, T) = \mathcal{T}_+ \exp\left(-i \int_{t_0}^T H_I(t) dt\right), \quad (4)$$

where \mathcal{T}_+ is the time-ordering operator. We approximate this integral as a product over small timesteps Δt (so that $\delta\Delta t \ll 1$) and take H_I to be constant throughout each step, so that

$$U(t_0, T) \approx \prod_{k=0}^{K-1} e^{-iV(x_I(k\Delta t))\Delta t}, \quad (5)$$

where $K = T/\Delta t$; we assume that, during the k th timestep, $H_I(t)$ is time independent and equals $V(x_I(k\Delta t))$.

To enact time evolution at step k , $V(x_I(k\Delta t))$ is expanded into a truncated Fourier series, whose terms correspond to the gates that synthesise the potential. Assuming the dynamics is confined to the region $x \in [-\Lambda/2, \Lambda/2]$, we expand V over this interval in a Fourier series,

$$V(x_I(k\Delta t)) \approx \sum_{n=1}^N B_n \cos\left(\frac{2\pi n}{\Lambda} x_I(k\Delta t) + \Phi_n\right), \quad (6)$$

where N is the number of Fourier terms, and B_n and Φ_n are the Fourier coefficients. The dynamics at the k th timestep is described by the operator

$$U(k\Delta t, (k+1)\Delta t) = e^{-iV(x_I(k\Delta t))\Delta t} \quad (7)$$

$$\approx \prod_{n=1}^N G_c^{(n)}(k\Delta t), \quad (8)$$

where we have approximated the unitary as a sequence of operators, and the approximation becomes exact in the limit $N \rightarrow \infty$ and $\Delta t \rightarrow 0$. $G_c^{(n)}$ is the *cosine trigonometric gate* [66]

$$G_c^{(n)}(k\Delta t) = \exp\left(-i\Delta t B_n \cos\left(\frac{2\pi n x_I(k\Delta t)}{\Lambda} + \Phi_n\right)\right). \quad (9)$$

Thus, the task of simulating any potential $V(x)$ of Eq. (1) amounts to implementing a series of cosine trigonometric gates. To simulate a single timestep, $G_c^{(n)}$ is applied N times, with the parameters of the gate corresponding to the parameters of the Fourier expansion in Eq. (6) (B_n , Φ_n and Λ).

Our implementation of $G_c^{(n)}(k\Delta t)$ is shown in Fig. 2b–c; it consists of a BQSP sequence, which is Trotterised to isolate the targeted cosine operator. We will now show that this sequence yields a cosine trigonometric gate. We begin with the CV–DV primitives that form the BQSP sequence, which consist of a state-dependent displacement (SDD)

$$D(\sigma_x \alpha) = \exp(\sigma_x(\alpha a^\dagger - \alpha^* a)) \quad (10)$$

and a single-qubit rotation (SQR)

$$R_\varphi(\vartheta) = \exp(-\frac{1}{2}i\vartheta \hat{\mathbf{n}}(\varphi) \cdot \boldsymbol{\sigma}), \quad (11)$$

where the complex number $\alpha = \alpha_0 e^{i\zeta}$ is given in terms of its magnitude, α_0 , and phase, $\zeta = \text{Arg}(\alpha)$, with $\alpha_0 \geq 0$ and $\zeta \in [0, 2\pi)$; ϑ is the angle of rotation, $\hat{\mathbf{n}} = (0, \sin \varphi, \cos \varphi)$ is the axis of rotation; and $\boldsymbol{\sigma} = (\sigma_x, \sigma_y, \sigma_z)$ is the vector of Pauli operators.

We construct a BQSP sequence [68] by placing an SQR operator between two SDDs,

$$Q(\alpha, \vartheta, \varphi) = D(-\sigma_x \alpha) R_\varphi(-\vartheta) D(\sigma_x \alpha), \quad (12)$$

which can be rewritten (see appendix A) as

$$Q(\alpha, \vartheta, \varphi) = \exp\left(\frac{1}{2}i\vartheta(\sigma_z \cos(2\sqrt{2}\alpha_0 x_\zeta + \varphi) + \sigma_y \sin(2\sqrt{2}\alpha_0 x_\zeta + \varphi))\right), \quad (13)$$

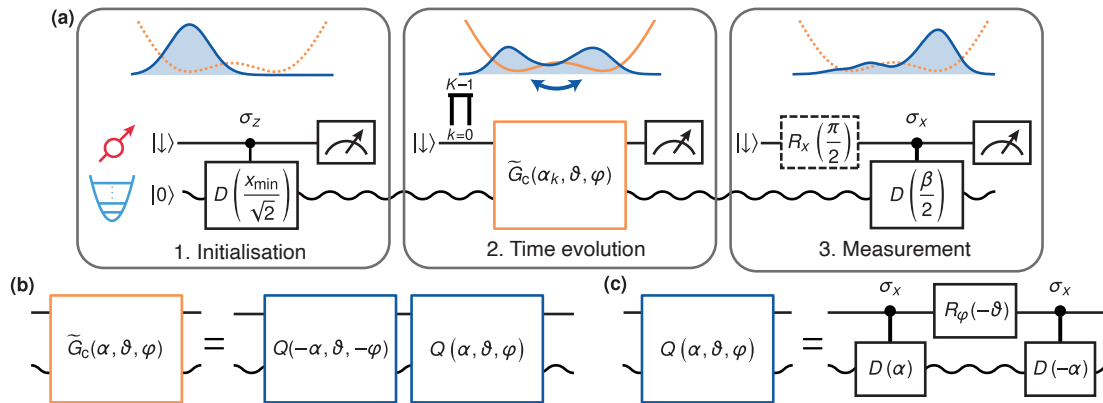


Figure 2. **Circuit diagram for simulating dynamics in double-well potentials.** (a) The experiment consists of three steps. 1. Initialisation of the wavepacket at a chosen position. The potential is a symmetric double well which is not synthesised at this stage (dotted line). The initial position is the minimum of the potential at $-x_{\min}$. 2. Time evolution of the wavepacket in the double-well potential (solid line) is simulated using the trigonometric gate, \tilde{G}_c . 3. Measurement of the oscillator state. Dashed box: optional operation to extract the imaginary part of the characteristic function. (b) The trigonometric gate is constructed with two BQSP subroutines. (c) The BQSP subroutine consists of two SDDs and an SQR.

where $x_\zeta = (ae^{-i(\zeta+\pi/2)} + a^\dagger e^{i(\zeta+\pi/2)})/\sqrt{2}$ is the rotated quadrature at phase $\zeta + \pi/2$.

Equation (13) contains the desired cosine operator for implementing $G_c^{(n)}$, as well as a term dependent on sine. We isolate the cosine term using the first-order Trotter decomposition [79]

$$e^{i(F+G)r} = e^{iFr} e^{iGr} + \mathcal{O}(r^2), \quad (14)$$

where F and G are operators and r is a small parameter. We set $e^{iFr} = Q(\alpha, \vartheta, \varphi)$, $e^{iGr} = Q(-\alpha, \vartheta, -\varphi)$ and take $\vartheta = r$, yielding a new operator which is the BQSP-implemented trigonometric gate conditioned on σ_z ,

$$\tilde{G}_c(\alpha, \vartheta, \varphi) = Q(\alpha, \vartheta, \varphi)Q(-\alpha, \vartheta, -\varphi) \quad (15)$$

$$= \exp(i\vartheta\sigma_z \cos(2\sqrt{2}\alpha_0 x_\zeta + \varphi)) + \mathcal{O}(\vartheta^2). \quad (16)$$

With an appropriate choice of parameters $(\alpha, \vartheta, \varphi)$, \tilde{G}_c realises the programmable target gate $G_c^{(n)}$. The qubit-dependence of \tilde{G}_c is removed by first preparing the qubit in an eigenstate of σ_z . Throughout this work, we initialise the qubit in $|\downarrow\rangle$. In particular, we implement

$$G_c^{(n)}(k\Delta t) = \langle\downarrow|\tilde{G}_c(\alpha, \vartheta, \varphi)|\downarrow\rangle, \quad (17)$$

by setting

$$\alpha = \frac{\pi n}{\sqrt{2}\Lambda} e^{ik\delta\Delta t}, \quad \vartheta = B_n \Delta t, \quad \varphi = \Phi_n, \quad (18)$$

and neglecting the $\mathcal{O}(\vartheta^2)$ term.

In the following sections, we use TGIFS to simulate the evolution of wavepackets in double-well potentials (see Fig. 1). Our target Hamiltonian is

$$H_{\text{sim}} = \frac{\delta}{2}(x^2 + p^2) + B \cos\left(\frac{2\pi x}{\Lambda} + \Phi\right), \quad (19)$$

which can be synthesised using TGIFS with a single Fourier component ($N = 1$). The corresponding potential is the sum of a harmonic term and a single trigonometric

component, which yields a double-well landscape near the origin. In this case, the evolution operator for the k th timestep is $\tilde{G}_c(\alpha_0 e^{i\zeta}, \vartheta, \varphi)$, where

$$\alpha_0 = \frac{\pi}{\sqrt{2}\Lambda}, \quad \zeta = k\delta\Delta t, \quad \vartheta = B\Delta t, \quad \varphi = \Phi. \quad (20)$$

Each of α_0 , ζ , ϑ , and φ can be experimentally adjusted, as detailed in Sec. II A, making the simulation programmable.

II. METHODS

A. Experimental implementation

We simulate the dynamics under H_{sim} using a trapped-ion system comprising an $^{171}\text{Yb}^+$ ion confined in a Paul trap [16, 80]. The bosonic (CV) information is encoded in one of the radial modes of motion, which has secular frequency $\omega_x = 2\pi \times 1.33$ MHz. The motional mode has negligible native anharmonicity due to the large ion-electrode distance (565 μm) [81]. Dephasing of the motional states occurs at a rate of $\gamma_\phi = 18\text{s}^{-1}$; the heating rate of 0.2 quanta s^{-1} [25] is comparatively insignificant [26]. The DV information is encoded in the hyperfine clock states of the $^2\text{S}_{1/2}$ level, with a qubit frequency $\omega_0 = 2\pi \times 12.6$ GHz. The qubit has a measured T_2^* time of 8.7 s [82], providing excellent coherence as a nonlinear element to engineer high-quality anharmonicity in the CV system.

Both the qubit and the oscillator are coherently controlled via stimulated Raman transitions, driven by two laser beams derived from a $\lambda = 355$ nm pulsed laser. The frequency, amplitude, phase and duration of the two beams are modulated independently by acousto-optic modulators. We operate in the Lamb-Dicke regime, $\eta^2(2\bar{n} + 1) \ll 1$, where \bar{n} is the average occupation number of the oscillator, which does not exceed 1.2 throughout the coherent evolution, and $\eta = 2\pi x_{\text{gnd}}/\lambda = 0.08$ is the Lamb-Dicke parameter. Here $x_{\text{gnd}} = \sqrt{\hbar/(2m\omega_x)} = 4.7$ nm is the spatial ex-

tent of the oscillator's ground-state wavefunction, where m is the ion's mass. Operation in the Lamb-Dicke regime allows driving sideband-resolving spin-motion interactions and neglecting higher-order (η^2 and higher) qubit-oscillator couplings.

Control of the qubit is achieved by tuning the frequency difference between the two beams to the qubit frequency. The interaction Hamiltonian after making the rotating-wave approximation is

$$H_Q = \frac{1}{2}\Omega_0\sigma_x, \quad (21)$$

where Ω_0 is the Rabi frequency. To realise the SQR $R_\varphi(\vartheta)$, we decompose it into three primitive rotations:

$$R_\varphi(\vartheta) = R_x(-\varphi)R_z(\vartheta)R_x(\varphi), \quad (22)$$

where $R_m(\theta) = \exp(-i\theta\sigma_m/2)$ for $m \in \{x, y, z\}$. $R_x(\varphi)$ is obtained by applying H_Q for time $\tau_\varphi = \varphi/\Omega_0$,

$$R_x(\varphi) = e^{-iH_Q\tau_\varphi}. \quad (23)$$

Arbitrary rotations in x and y can be applied with other choices of times and phases. $R_z(\vartheta)$ rotations are implemented by shifting the phase of the qubit's reference local oscillator during the SQR pulse and for all subsequent operations.

Coherent qubit-oscillator operations are driven by tuning the frequency difference between the two Raman beams close to the motional sidebands of the carrier transition. We drive red-sideband (RSB) and blue-sideband (BSB) interactions,

$$H_{\text{RSB}} = \frac{1}{2}i\Omega(a\sigma_+e^{i(\delta_L t - \phi_r)}) + \text{h.c.} \quad (24)$$

$$H_{\text{BSB}} = -\frac{1}{2}i\Omega(a\sigma_-e^{i(\delta_L t + \phi_b)}) + \text{h.c.}, \quad (25)$$

where $\Omega = \eta\Omega_0$ is the Rabi frequency of the sideband transitions, δ_L is the laser detuning from the motional sideband frequency, $\sigma_\pm = (\sigma_x \pm i\sigma_y)/2$ are the qubit raising (+) and lowering (-) operators, and ϕ_r and ϕ_b are the relative phases of the light for the RSB and BSB, respectively. Driving both interactions simultaneously couples the spin to the motion with the Hamiltonian

$$H_{\text{SDD}} = H_{\text{RSB}} + H_{\text{BSB}} \quad (26)$$

$$= -\frac{\Omega}{2}\sigma_{\phi_s}(ae^{i(\phi_m + \delta_L t)}) + \text{h.c.}, \quad (27)$$

where $\sigma_{\phi_s} = \sigma_x \cos \phi_s + \sigma_y \sin \phi_s$, $\phi_s = (\phi_r + \phi_b)/2$ and $\phi_m = (\phi_b - \phi_r)/2$ are the qubit and the oscillator phases, respectively.

By setting $\delta_L = 0$, $\phi_s = 0$ and $\phi_m = \pi/2$, driving H_{SDD} for a duration τ implements the SDD

$$e^{-iH_{\text{SDD}}\tau} = D\left(\frac{1}{2}\sigma_x\Omega\tau\right). \quad (28)$$

B. Pulse sequence

The experiment simulates the dynamics of a wavefunction within a double-well potential by implementing the above control and by performing tomography to reconstruct the motional wavepacket throughout its evolution.

We set the parameters of the target Hamiltonian H_{sim} to resolve tunnelling dynamics within experimentally accessible operating conditions. Initially, we investigate a

symmetric double well, with minima located at $\pm x_{\text{min}} = \pm 1.5$. We set $\alpha_0 = \pi/6$, $\delta = 2\pi \times 500$ Hz, $\vartheta = 0.8$, and $\varphi = 0$, which yields a symmetric double-well potential, and the barrier height is $V(0) - V(x_{\text{min}}) = 0.93\delta$.

The experiment is separated into three steps, depicted in Fig. 2: *initialisation* of the wavepacket at the desired location; *time evolution* using the trigonometric gate to simulate dynamics; and *measurement* of the final state.

1. Initialisation

We first prepare the oscillator in the ground state with a mean occupation of 0.04 quanta by Doppler cooling followed by sideband cooling. The qubit is prepared in $|\downarrow\rangle$ by optical pumping. See appendix B for details.

Next, we displace the wavepacket from the origin to the desired initial position at the centre of the left well (at $-x_{\text{min}}$). To do this, we implement a three-pulse sequence. We first apply a rotation $R_y(\pi/2)$ to transfer the qubit into the $|+\rangle$ eigenstate of σ_x . Next, we apply the SDD $D(-\sigma_x x_{\text{min}}/\sqrt{2})$. Finally, $R_y(-\pi/2)$ returns the qubit to $|\downarrow\rangle$.

We apply a mid-circuit measurement on the qubit to reduce erroneous spin flips during state preparation (see appendix C). A measurement outcome of $|\uparrow\rangle$ implies an error in the initialisation procedure, and the result of the experiment is ignored. Our initialisation procedure measures a successful $|\downarrow\rangle$ outcome on $> 99\%$ of experimental shots, a value comparable with our state-preparation and measurement fidelities.

2. Time evolution

Following initialisation, we apply the trigonometric gate \tilde{G}_c K times to implement stepwise evolution under H_{sim} for total duration $K\Delta t$. The state $|\psi(0)\rangle$ evolves according to

$$|\psi(K\Delta t)\rangle = \left(\prod_{k=0}^{K-1} \tilde{G}_c(\alpha_0 e^{i\zeta}, \vartheta, \varphi) \right) |\psi(0)\rangle, \quad (29)$$

with parameter values given in Eq. (20). We implement \tilde{G}_c using the sequence of SQR and SDD operations shown in Fig. 4. We set $\phi_s = 0$. To realise the given α_0 and φ , we choose the SDD pulse duration τ and the SQR duration τ_φ so that

$$\tau = \frac{2\alpha_0}{\Omega} \quad \text{and} \quad \tau_\varphi = \frac{\varphi}{\Omega_0}, \quad (30)$$

where Rabi frequencies $\Omega_0 = \pi/35$ μs and $\Omega = \pi/150$ μs are determined by the laser intensity at the ion. Hence, for the targeted double-well potential with parameters stated above, we choose $\tau = \Delta t/4 = 50$ μs and $\tau_\varphi = 0$. ϑ is realised using an R_z rotation, as described in Sec. II A. The phase $\zeta = \delta k\Delta t$ in \tilde{G}_c increases with the timestep k . This increase is implemented through H_{SDD} (Eq. (27)) where we set ϕ_m to be constant and $\delta_L = -\delta = -2\pi \times 500$ Hz.

After time evolution, we perform a second mid-circuit measurement, and post-select on $|\downarrow\rangle$ outcomes. The derivation of H_{sim} in Sec. I assumed that the qubit remains

in $|\downarrow\rangle$ throughout the evolution. However, Trotter errors in Eq. (16) can lead to spin flips. By rejecting spin-flip outcomes, the mid-circuit measurement mitigates these errors.

3. Measurement

The state of the oscillator is measured at various points throughout the evolution under the double-well potential. The motional state is measured by first entangling with the qubit followed by projective qubit measurements. We extract the characteristic function $\chi(\beta) = \langle D(\beta) \rangle$, where the expectation value is taken with respect to the motional state [83]. This approach can be used for both full tomography (allowing the reconstruction of the state's Wigner function, $W(x, p)$) as well as measurements that directly give information such as the probability distributions $P(x)$ or the expectation values of quadratures.

The measurement protocol is depicted in Fig. 2a. We measure $\chi(\beta)$ by applying the SDD $D(\sigma_x \beta / 2)$, followed by a qubit measurement in the computational (σ_z) basis (see appendix C). The expectation value of the measurement gives the real part of the characteristic function, $\langle \sigma_z \rangle = \text{Re}[\chi(\beta)]$. Prepending $R_x(\pi/2)$ (dashed box) gives the imaginary part, $\langle \sigma_z \rangle = \text{Im}[\chi(\beta)]$. These expectation values are estimated by repeating the measurement procedure and averaging the results. This is repeated for all desired values of β . Due to the Hermitian symmetry $\chi(-\beta) = \chi(\beta^*)$, scanning half of the phase space is sufficient to fully construct $\chi(\beta)$.

Representative results of this measurement are shown for a symmetric double well in Fig. 3a–b at $t = 4$ ms, which corresponds to the time it takes the wavepacket to tunnel to the opposite side of the barrier. A Fourier transform of $\chi(\beta)$ gives the Wigner function (Fig. 3c)

$$W(x, p) = \frac{1}{\pi^2} \int d^2\beta \chi(\beta) e^{\gamma\beta^* - \gamma^*\beta}, \quad (31)$$

where $\gamma = (x + ip)/\sqrt{2}$. The probability distribution of the state can be obtained through the integral of $W(x, p)$ along the orthogonal axis. For example, the position probability distribution is given by,

$$P(x) = \int_{-\infty}^{\infty} W(x, p) dp, \quad (32)$$

which is shown in (Fig. 3d).

The distribution $P(x)$ can also be reconstructed from fewer measurement samples by performing a one-dimensional scan of $\chi(\beta)$ with $\text{Re}[\beta] = 0$,

$$P(x) = \frac{1}{2\pi} \int_{-\infty}^{\infty} du e^{-iux} \chi\left(\frac{i u}{\sqrt{2}}\right). \quad (33)$$

In this approach, the number of measurements of $\chi(\beta)$ is reduced compared to integrating $W(x, p)$.

The expectation value of a quadrature can be extracted with even fewer measurements by estimating the slope of the characteristic function at the origin [31]. In particular, $\langle x \rangle$ is given by [84],

$$\langle x \rangle = \frac{1}{\sqrt{2}} \left. \frac{\partial \text{Im}[\chi(\beta)]}{\partial \text{Im}[\beta]} \right|_{\beta=0}. \quad (34)$$

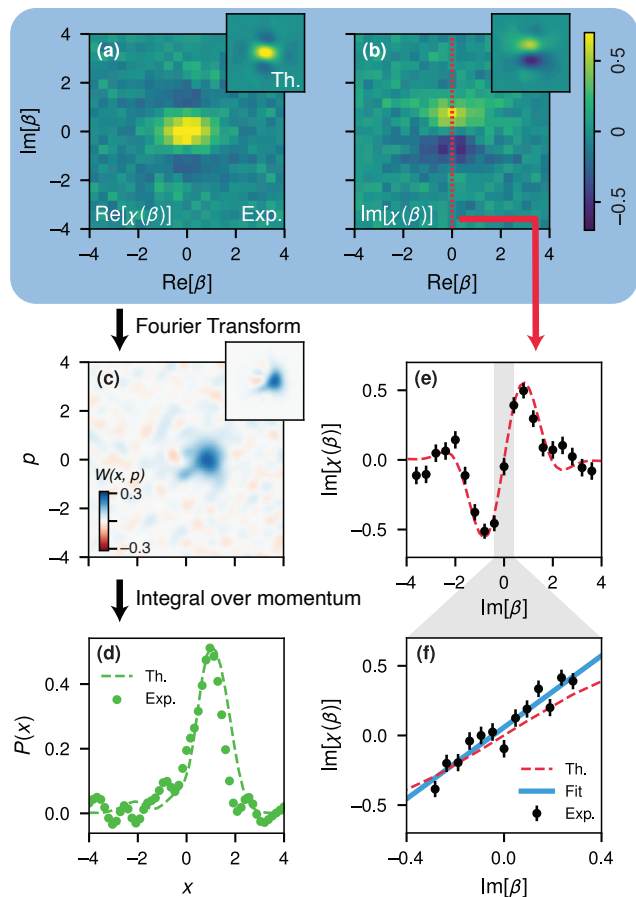


Figure 3. **Reconstruction of motional wavepackets and extraction of position expectation values.** Given are representative measurements at $t = 4$ ms for a symmetric double well. (a,b) Real and imaginary parts of the characteristic function $\chi(\beta)$. (c) Wigner function $W(x, p)$ obtained as the Fourier transform of $\chi(\beta)$. (d) Probability distribution $P(x)$, obtained as $\int dp W(x, p)$. (e) Slope of $\text{Im}[\chi(\beta)]$ at $\text{Im}[\beta] = 0$ determines $\langle x \rangle$ (Eq. (34)). (f) Finer measurement of $\partial \text{Im}[\chi(\beta)] / \partial \text{Im}[\beta]$ to determine $\langle x \rangle$. All theoretical models include dephasing and Trotter error.

In our measurement, we fit a line to experimental data points to determine $\langle x \rangle$ (see Fig. 3f).

We can also extract $\langle x \rangle$ by measuring only one value of $\chi(\beta)$ and finding the slope at the origin from two-point finite difference (2PFD). For the two points, we take the first to be at the origin, $\text{Im}[\chi(0)] = 0$ (because $\chi(0) = 1$), and the second to be $\text{Im}[\chi(ih)]$. When h is sufficiently small, χ can be treated as linear, and the expectation value is found by approximating Eq. (34) as

$$\langle x \rangle \approx \frac{\text{Im}[\chi(ih)]}{\sqrt{2}h}. \quad (35)$$

This scheme requires a suitable choice of h : if h is too small, the quantum projection noise will be greater than $\text{Im}[\chi(ih)]$ (for a given number of measurements) and if h is too large, error arises due to nonlinearity in $\chi(\beta)$. We use $h = 0.4$ throughout this work, which was chosen because it ensures the total error from shot noise and the 2PFD is small compared to other errors, as shown in appendix D.

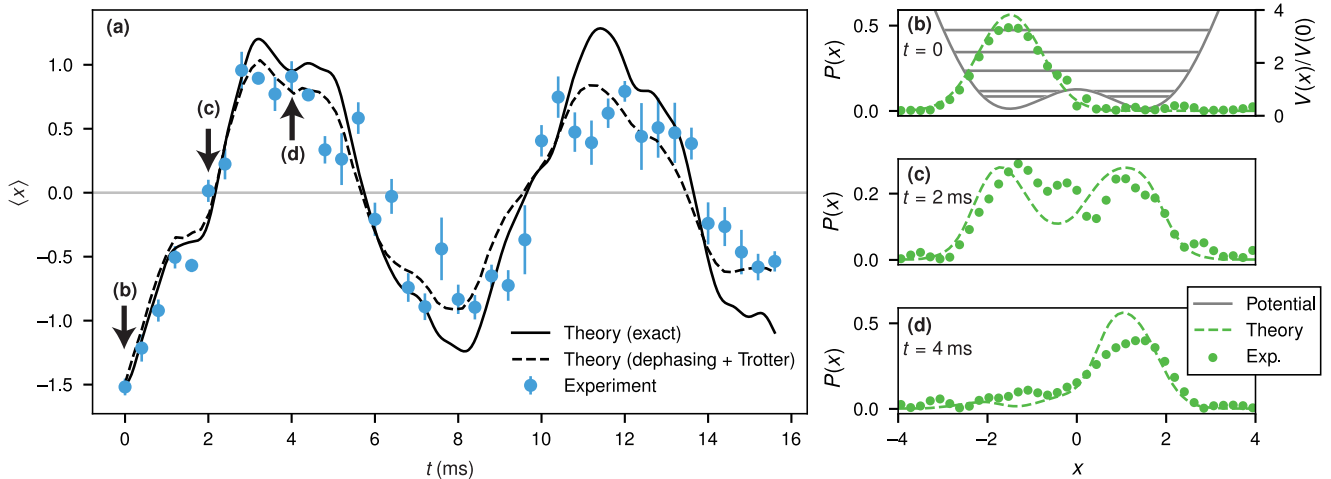


Figure 4. **Quantum tunnelling in a synthesised symmetric double-well potential.** (a) Expectation value $\langle x \rangle$ of the wavepacket’s position through time, showing oscillations due to tunnelling through the barrier centred at $x = 0$. Experimental points are determined as in Fig. 3f, with error bars obtained from the uncertainty in the slope of the fit line. We also show the theoretical predictions for the exact dynamics under H_{sim} (solid line) and including dephasing and Trotter error (dashed line). (b–d) Reconstructed probability distributions $P(x)$ at $t = 0$ ms, $t = 2$ ms and 4 ms, compared with theoretical predictions (including both dephasing and Trotter error). Also shown in (b) is the target potential and the associated energy levels. The combined probability of occupying the two lowest levels (both below the barrier) is 95%.

III. RESULTS

We simulate the double-well potential defined by H_{sim} using the trigonometric gate to implement the evolution and observe tunnelling dynamics. First, we simulate a symmetric double well and measure $\langle x \rangle$ as a function of time, observing tunnelling through the barrier. Second, we tune experimental parameters to programmably introduce asymmetry, which suppresses the tunnelling. In all simulated potentials, we observe good agreement between experiment and theory.

A. Symmetric double well

Wavepacket tunnelling in the symmetric double well behaves as expected, see Fig. 4a. The wavepacket is initialised in the left well as described in Sec. IIB 1. As time evolves, the slow oscillation of $\langle x \rangle$ indicates that the wavepacket tunnels through the barrier four times in 16 ms. We observe good agreement between the experiment and the theory. In particular, we observe only partial revivals, that is, the wavepacket does not return to its initial spatial profile because of the population in states with energies above the barrier. The deviations from the exact dynamics are accounted for by errors dominated by motional dephasing, Trotter error, and measurement imperfections (see appendix D).

Figure 4b–d shows the reconstructed wavepacket probability distributions $P(x)$ at three times, revealing the localisation of the wavepacket in each well at the turning points of the oscillation ($t = 0$ and $t = 4$ ms), as well as its delocalisation across the two wells at an intermediate time ($t = 2$ ms). Appendix E gives the complete data for $\chi(\beta)$ used to construct these probabilities, as well as further validation by scanning the entire characteristic function. Results for $t = 4$ ms are highlighted in Fig. 3.

B. Asymmetric double wells

We demonstrate the programmability of our scheme by simulating several asymmetric double-well potentials and different initial conditions. To do so, we tune the parameters in Eq. (16), which necessitates the implementation of $R_x(\varphi)$, which was not needed for the symmetric well. We quantify the asymmetry of our double-well potentials using the ratio of the wells’ depths measured from the top of the barrier. That is, the amount of asymmetry is

$$\Xi = 1 - \frac{V(x_{\text{max}}) - V(x_{\text{min},1})}{V(x_{\text{max}}) - V(x_{\text{min},2})}, \quad (36)$$

where $x_{\text{min},1}$ and $x_{\text{min},2}$ are the local minima of the left and right wells, respectively, and x_{max} is the local maximum between them. For symmetric double wells, $\Xi = 0$, corresponding to setting $\varphi = 0$.

In each simulation, we measured $\langle x \rangle$ using 2PFD with $h = 0.4$ and with 200 measurements per point (as validated in appendix D).

The observed dynamics are shown in Fig. 5. We first replicate the symmetric double-well simulation in Fig. 4, but this time estimating the wavepacket position using the 2PFD measurement, showing good agreement with theory. We then break the symmetry of the double-well potential by varying φ in Fig. 5b–e. The results demonstrate how the strength of the asymmetry affects the tunnelling dynamics. In Fig. 5b,c,d, we introduce an asymmetry of $\Xi = -0.14$. The asymmetry means that the eigenstates of the potential are no longer symmetric, and so the initial state is not in an equal superposition of the two lowest eigenstates, which has the effect of suppressing the tunnelling. Whether the wavepacket starts in the left or the right well, the amplitude of the oscillations in $\langle x \rangle$ is smaller than the oscillation for the symmetric double well. In Fig. 5d, the wavepacket is initialised in the centre of the asymmetric potential,

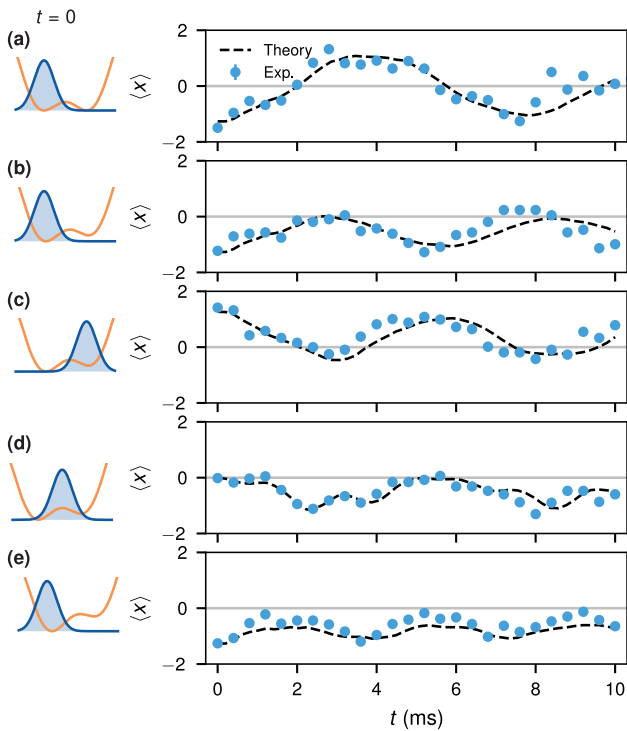


Figure 5. **Programmable anharmonic dynamics.** Wavepacket evolution for various potentials and initial states. Position expectation values $\langle x \rangle$ are extracted, as functions of time, by 2PFD (Eq. (35) with $h = 0.4$). To engineer asymmetric potentials, we vary the trigonometric-gate angle φ from (a) $\varphi = 0$ to (b,c,d) $\varphi = -\pi/20$ and (e) $\varphi = -\pi/10$. Error bars derived from spin-measurement noise are smaller than the data markers. Theory includes dephasing, Trotter, and 2PFD errors.

reflecting the greater overlap of the initial state with the lowest eigenstate. In Fig. 5e, we increase the asymmetry to $\Xi = -0.31$, further suppressing the tunnelling.

IV. DISCUSSION

We demonstrate a programmable quantum simulation of anharmonic dynamics using a trapped-ion CV–DV device. Our approach uses TGIFS to compile a target anharmonic potential into a sequence of non-Gaussian gates, which are decomposed into primitive gates commonly available in current CV–DV devices. We synthesise a symmetric double-well potential and demonstrate coherent wavepacket dynamics of tunnelling. To demonstrate programmability, we adjust programmable experimental parameters such as laser phases and pulse durations, synthesising a range of double-well potentials with controllable asymmetries and observing suppression of wavepacket tunnelling.

Our experiment uses the long-lived native coherence of both the DV and CV degrees of freedom in trapped-ion systems. We use light-atom interactions to implement fully tunable, high-quality CV–DV primitives. We implement as many as 312 CV–DV entangling gates (state-dependent displacements with magnitude $\alpha_0 = \pi/6$ per gate) and observe coherent dynamics up to 16 ms.

Looking forward, we envision four complementary

routes to expand the range and capability of programmable anharmonic simulations.

Increased accuracy and complexity. Increasing the number of Trotter steps or Fourier terms improves the accuracy or the complexity of the potential at the cost of additional circuit depth. Currently, our circuit depth is limited by gate times and the motional dephasing rate. These can be improved with stronger light-atom coupling and improved stabilisation of motional frequency. Higher-order Fourier series could be used to implement, for example, quartic [66] and Morse [64] potentials, as well as higher-order vibronic couplings for molecular simulation [10].

Time-dependent Hamiltonians. TGIFS natively supports simulation of time-dependent Hamiltonians. Time dependence can be implemented by updating the control parameters from one timestep to the next, which would enable quantum simulations of laser-driven chemical reactions [85], and chaotic systems [36].

Multimode scaling. Implementing multimode TGIFS by interleaving trigonometric gates across motional modes allows simulations of nonlinear couplings [66]. Large Coulomb crystals [5, 86] provide multiple frequency-resolved motional modes, offering opportunities to simulate problems that scale unfavourably on classical computers [87].

Engineered dissipation. TGIFS is, in principle, compatible with the existing framework for simulating open quantum systems by controlled noise injection [16, 28, 29, 88]. This opens opportunities to simulate dissipative anharmonic dynamics in molecular systems such as proton transfer in the condensed phase [89, 90], energy transport [91, 92] and bond breaking [93, 94].

Overall, our experiment validates TGIFS as a framework for simulating anharmonic potentials, provides an experimental demonstration of BQSP, and establishes it as a practical framework for implementing programmable non-Gaussian operations. Extending our approach as detailed above would broaden the class of anharmonic dynamics accessible to CV–DV simulators, enabling high-throughput simulations of physical models spanning applications from quantum chemistry to condensed-matter and high-energy physics.

ACKNOWLEDGMENTS

We thank Julian Jee for his feedback on the manuscript. We were supported by the U.S. Office of Naval Research Global (N62909-24-1-2083), the U.S. Air Force Office of Scientific Research (FA2386-23-1-4062), the Wellcome Leap Quantum for Bio program, the Australian Research Council (FT220100359, FT230100653), Lockheed Martin, the Sydney Quantum Academy (MJM, NP), the University of Sydney Postgraduate Award scholarship (VGM), the Australian Government Research Training Program (FS), the Sydney Horizon Fellowship (TRT), and H. and A. Harley.

AUTHOR CONTRIBUTIONS STATEMENT

CM, TC, KS, VGM, CHV, IK, TRT conceived the idea. CM, FS, TC, KS developed the experimental protocols. CM performed the experiment. CM, TC analysed the data. CM, FS, MJM, VGM, CHV, PN, HKC, TRT contributed to the experimental apparatus, and TC, KS provided theoretical support. IK and TRT supervised the project. CM, TC, KS, IK, TRT wrote the manuscript. All authors provided suggestions for the experiment, discussed the results, and contributed to the manuscript.

COMPETING INTERESTS STATEMENT

The authors declare no competing interests.

DATA AVAILABILITY

A repository containing the experimental data presented in this article is available at Ref. [95]

APPENDICES

Appendix A: Generating trigonometric gates

Here, we provide the derivation of the operator $Q(\alpha, \vartheta, \varphi)$ constructed with a BQSP sequence consisting of a single-qubit rotation and two state-dependent displacement operators. We begin with the simple case of $\varphi = 0$, which is used to synthesise the symmetric double-well potential. We begin the derivation by rewriting Eq. (12) as

$$Q(\alpha, \vartheta, 0) = D(-\sigma_x \alpha) e^{i\vartheta \sigma_z / 2} D(\sigma_x \alpha) \quad (\text{A1})$$

$$= \exp\left(\frac{1}{2} i \vartheta D(-\sigma_x \alpha) \sigma_z D(\sigma_x \alpha)\right). \quad (\text{A2})$$

where we use the fact that $D(\sigma_x \alpha)$ is unitary and $D(-\sigma_x \alpha) = D^\dagger(\sigma_x \alpha)$.

Equation (A2) can be simplified using the identity

$$e^{i\Theta \sigma_x} \sigma_z e^{-i\Theta \sigma_x} = \cos(2\Theta) \sigma_z + \sin(2\Theta) \sigma_y, \quad (\text{A3})$$

which holds when Θ is Hermitian and $[\Theta, \sigma_z] = 0$. In our case, $\Theta = -i(\alpha a^\dagger - \alpha^* a)$, which yields

$$Q(\alpha, \vartheta, 0) = \exp\left(\frac{1}{2} i \vartheta (\sigma_z \cos(2\sqrt{2}\alpha_0 x_\zeta) + \sigma_y \sin(2\sqrt{2}\alpha_0 x_\zeta))\right), \quad (\text{A4})$$

which is then used to synthesise a trigonometric gate $\tilde{G}_c(\alpha, \vartheta, 0)$ to simulate anharmonic dynamics in a symmetric double-well potential.

This approach is straightforwardly extended to asymmetric double wells. Here, we have a nonzero φ in the BQSP operation $Q(\alpha, \vartheta, \varphi)$ defined in Eq. (12),

$$\begin{aligned} Q(\alpha, \vartheta, \varphi) &= D(-\sigma_x \alpha) R_\varphi(-\vartheta) D(\sigma_x \alpha), \\ &= D(-\sigma_x \alpha) R_x(-\varphi) R_z(\vartheta) R_x(\varphi) D(\sigma_x \alpha). \end{aligned} \quad (\text{A5})$$

Because the R_x rotations commute with $D(\sigma_x \alpha)$, their orders can be swapped to rewrite Eq. (A5) as

$$Q(\alpha, \vartheta, \varphi) = R_x(-\varphi) Q(\alpha, \vartheta, 0) R_x(\varphi). \quad (\text{A6})$$

As the rotation operators are unitary, they can be moved inside the exponent of $Q(\alpha, \vartheta, 0)$ (Eq. (A4)),

$$\begin{aligned} Q(\alpha, \vartheta, \varphi) &= \exp\left(\frac{1}{2} i \vartheta (R_x(-\varphi) \sigma_z R_x(\varphi) \cos(2\sqrt{2}\alpha_0 x_\zeta) \right. \\ &\quad \left. - R_x(-\varphi) \sigma_y R_x(\varphi) \sin(2\sqrt{2}\alpha_0 x_\zeta))\right). \end{aligned} \quad (\text{A7})$$

Here, we apply Eq. (A3) to $R_x(-\varphi) \sigma_z R_x(\varphi)$ inside the exponent, with $\Theta = \varphi/2$. We use a similar identity for $R_x(-\varphi) \sigma_y R_x(\varphi)$. Finally, gathering trigonometric terms gives Eq. (13).

Appendix B: State preparation

As part of the experimental initialisation, we prepare the ion's spin and motional ground states in three steps.

First, we apply Doppler cooling to the ion using a 369.5 nm laser that is red-detuned from the Yb^+ ion's $^2\text{S}_{1/2} \rightarrow ^2\text{P}_{1/2}$ transition. This laser is aligned with components along all trap axes, cooling all motional modes.

Second, radial modes are cooled to their motional ground states with pulsed sideband cooling [96], using the same 355 nm laser described in Sec. II. We cool both radial modes; the axial mode is not cooled as it is inaccessible due to our laser beam geometry. We typically reach an average phonon number of $\bar{n} = 0.04$, verified by sideband thermometry [97].

Third, the spin is prepared in the ground state by optically pumping on resonance with the $^2\text{S}_{1/2} |F=1\rangle \rightarrow ^2\text{P}_{1/2} |F=1\rangle$ transition.

Appendix C: Qubit measurement

We determine the state of the qubit by fluorescence measurement of the $|\uparrow\rangle$ state by driving the $^2\text{S}_{1/2} |F=1\rangle \rightarrow ^2\text{P}_{1/2} |F=0\rangle$ transition. Scattered light is collected by a high-numerical-aperture imaging system and focused onto an avalanche photodiode. The qubit state is inferred from the number of scattered photons via thresholding: photon counts higher than a pre-calibrated threshold indicate the $|\uparrow\rangle$ (bright) state, while counts lower than the threshold give the $|\downarrow\rangle$ (dark) state. We use a measurement duration of 250 μs and a photon threshold of two.

We post-select results based on two mid-circuit measurements that yield binary outcomes; if a bright state is detected at either measurement, the result is discarded. Only keeping the dark state suppresses photon scattering by the ion during the mid-circuit measurements, thereby avoiding the effects of photon recoil on the motional state. Mid-circuit measurements are performed for 50 μs , with a threshold of one photon. The outcome is stored in a buffer memory of our experimental control hardware and read out at the end of the entire sequence (after the final measurement).

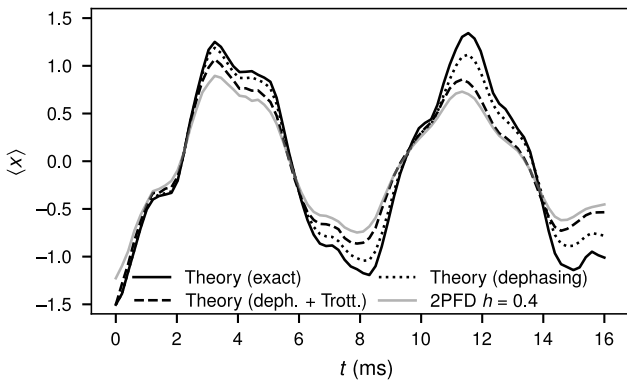


Figure 6. **Errors due to dephasing, Trotter error and 2PFD measurement.** Traces show the effect as additional error sources are added to the theoretical model of our simulation of a symmetric double well. Shown are: exact theoretical dynamics described by H_{sim} , theoretical dynamics including dephasing, theoretical dynamics including both dephasing and Trotter error, and theoretical dynamics with dephasing, Trotter error and 2PFD readout error for $h = 0.4$.

Appendix D: Sources of error

Three main error sources cause deviation of experimental results from the exact dynamics: experimental noise (which is dominated by motional dephasing), Trotter error and errors associated with the two-point finite difference (2PFD) measurement scheme.

Dephasing occurs due to amplitude fluctuations of the radio-frequency signal that generates the trapping potential [26, 96]. To combat this, the amplitude is locked to a reference voltage via a proportional-integral-derivative feedback loop [10] and the remaining slow fluctuations are partially mitigated by periodically recalibrating the motional frequencies during each experimental run. Dephasing is modelled by solving the Lindblad master equation for H_{sim} with the Lindblad operator $L_{\gamma_\phi} = \sqrt{\gamma_\phi} a^\dagger a$, where $\gamma_\phi = 18 \text{ s}^{-1}$ is the measured dephasing rate.

Trotter error associated with our approximation of \tilde{G}_c in Eq. (16) leads to further deviation from the target dynamics. The error can be separated into two. This first is the $\mathcal{O}(\vartheta^2)$ term in Eq. (16), which could be reduced by a higher-order Trotter expansion or a shorter timestep [66]. Spin flips associated with this Trotter error are mitigated by the mid-circuit measurement, as described in Sec. II B 2. The second error arises from setting a static laser detuning δ_L in H_{SDD} (Eq. (27)) to implement the phase increment in \tilde{G}_c . This error be-

Table I. **SRMSE due to dephasing, Trotter error and 2PFD measurement.** The effect of each error with respect to the previous in isolation, as well as cumulative SRMSE from the ideal case, corresponding to the numerical results in Fig. 6.

Source	SRMSE (%)	Cumulative SRMSE (%)
Dephasing	13.6	13.6
Trotter	19.2	29.8
2PFD ($h = 0.4$)	3.7	31.9

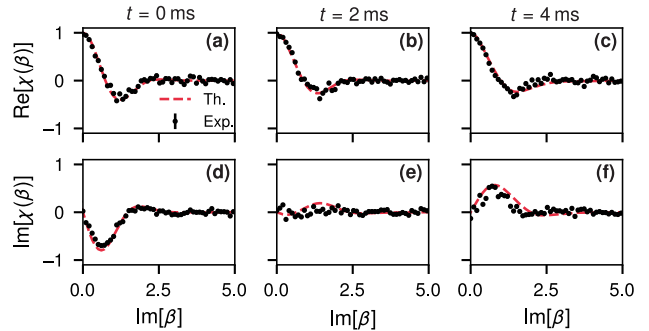


Figure 7. **Measured characteristic function** used to construct the probability densities in Fig. 4. (a–c) The real parts of $\chi(\beta)$ at $t = 0 \text{ ms}$, 2 ms and 4 ms , respectively. (d–f) Corresponding imaginary parts. Theoretical predictions (including dephasing and Trotter error) are given for comparison. The error bars correspond to measurement projection noise, and are smaller than the points. We measure $\chi(\beta)$ at 50 points in the range $\text{Im}[\beta] \in [0, 5]$ in randomised order, with 500 measurements per point.

comes negligible in the limit of $|\delta_L|\tau \ll 1$. Trotter error is included in the simulation by solving the Lindblad master equation with dephasing Lindbladian operator L_{γ_ϕ} for the complete pulse sequence of SDD and SQR primitives at each timestep.

The 2PFD slope measurement scheme used to extract the data in Fig. 5 introduces an error that depends on h , the distance of the sample point from the origin. The scheme demands that h is chosen to be sufficiently small, so that the second measurement point is taken in the regime where $\text{Im}[\chi(\beta)]$ remains linear.

Figure 6 plots dynamics with these errors and Table I quantifies the scaled root-mean-square error (SRMSE) for each error source. For two series of length M , $a = \{a_k\}$ and $b = \{b_k\}$, the SRMSE is

$$\epsilon(a, b) = \sqrt{\frac{\sum_{k=1}^M (a_k - b_k)^2}{\sum_{k=1}^M a_k^2}}. \quad (\text{D1})$$

The first column of Table I reports the incremental SRMSE obtained when successive error mechanisms are included (e.g., theory with dephasing versus the exact solution; theory with dephasing and Trotterisation versus theory with dephasing; etc.). The second column reports the SRMSE of each model when compared to the exact solution. The experimental data deviate from the exact dynamics largely because of the dephasing and Trotter errors, with 2PFD errors being relatively minor at our choice of $h = 0.4$.

Appendix E: Motional state measurement

In this section, we present further measurements of the oscillator state in the symmetric double-well case.

Fig. 7 shows characteristic function $\chi(\beta)$ measurements that are used to construct the probability distributions in Fig. 4.

In addition, we perform a full two-dimensional scan of $\chi(\beta)$ at $t = 0 \text{ ms}$, 2 ms , and 4 ms (see Fig. 8). We

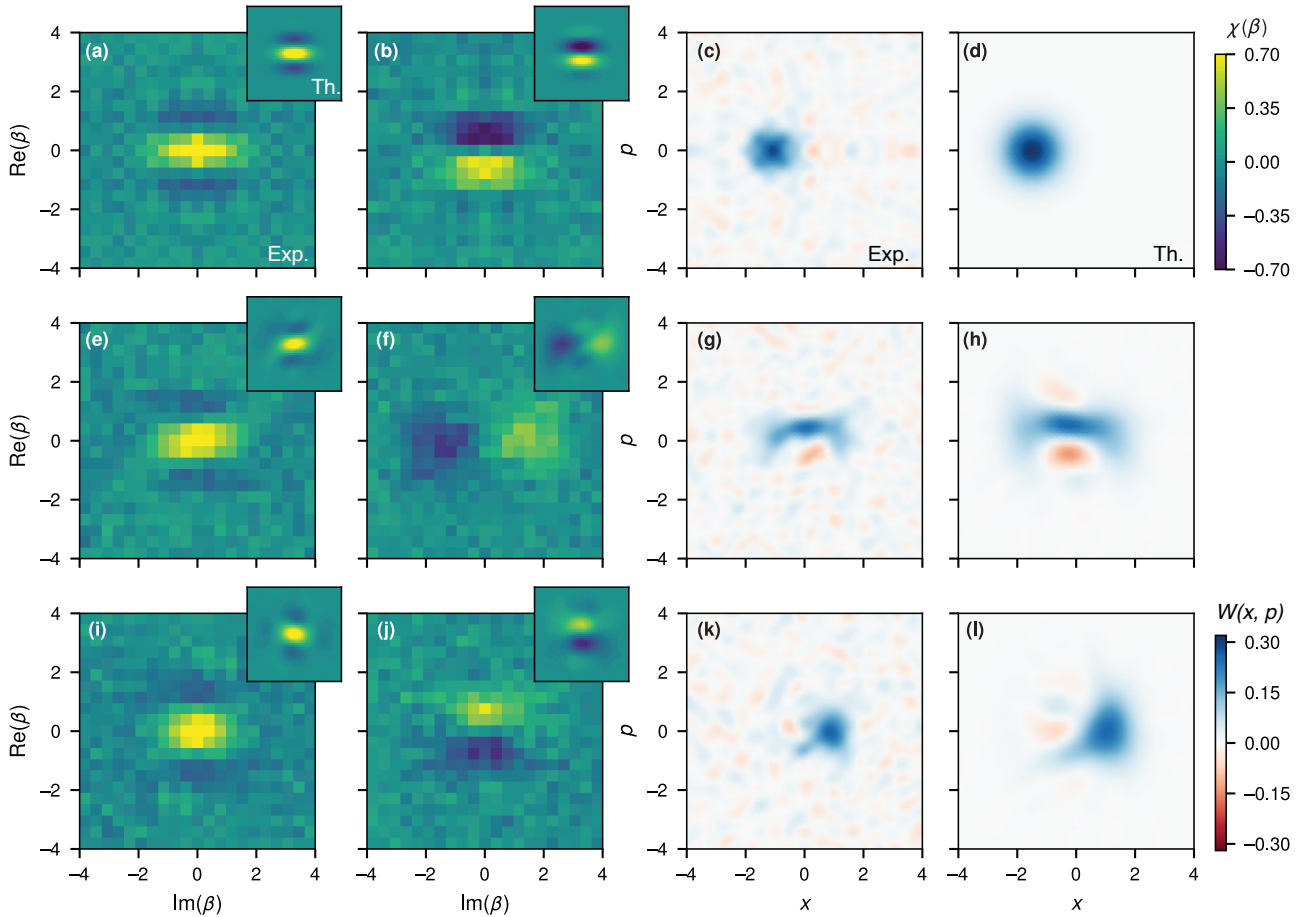


Figure 8. **Two-dimensional scans of the characteristic and reconstructed Wigner functions for the symmetric double well**, supplementing the data in Fig. 4. (a) $\text{Re}[\chi(\beta)]$ at $t = 0$ ms, measured on a 21×21 grid. Inset: theoretical $\text{Re}[\chi(\beta)]$ with dephasing and Trotter error. (b) The corresponding imaginary part of $\chi(\beta)$. (c) Measured Wigner function $W(x, p)$ at $t = 0$ ms. (d) Theoretical $W(x, p)$ with dephasing and Trotter error. The next two rows show the same plots at $t = 2$ ms ((e)–(h)) and $t = 4$ ms ((i)–(l)).

measure $\chi(\beta)$ in the range $\text{Re}[\beta] \in [-4, 4]$ (21 points) and $\text{Im}[\beta] \in [0, 4]$ (11 points), and use the symmetry of χ to determine the unmeasured values. At $t = 0$, measuring only the real quadrant is sufficient to determine χ because the prepared state is even in momentum, i.e., $\chi(\beta) = \chi(\beta^*)$. The data are collected in a random order

with 250 measurements per point. Wigner functions are obtained from the Fourier transform of $\chi(\beta)$ using Eq. (31). When calculating $W(x, p)$, $\chi(\beta)$ data are padded with zeros (out to $|\text{Re}[\beta]| < 10$ and $|\text{Im}[\beta]| < 10$), and the background is subtracted from each $\chi(\beta)$ (mean value $(-5.0 + 0.1i) \times 10^{-3}$) [26].

* cameron.mcgarry@sydney.edu.au

† tingrei.tan@sydney.edu.au

- [1] R. P. Feynman, *Int. J. Theor. Phys.* **21**, 467 (1982).
- [2] S. Lloyd, *Science* **273**, 1073 (1996).
- [3] I. M. Georgescu, S. Ashhab, and F. Nori, *Rev. Mod. Phys.* **86**, 153 (2014).
- [4] J. Zhang, G. Pagano, P. W. Hess, A. Kyprianidis, P. Becker, H. Kaplan, A. V. Gorshkov, Z.-X. Gong, and C. Monroe, *Nature* **551**, 601 (2017).
- [5] S.-A. Guo, Y.-K. Wu, J. Ye, L. Zhang, W.-Q. Lian, R. Yao, Y. Wang, R.-Y. Yan, Y.-J. Yi, Y.-L. Xu, B.-W. Li, Y.-H. Hou, Y.-Z. Xu, W.-X. Guo, C. Zhang, B.-X. Qi, Z.-C. Zhou, L. He, and L.-M. Duan, *Nature* **630**, 613 (2024).
- [6] M. Meth, J. Zhang, J. F. Haase, C. Edmunds, L. Postler, A. J. Jena, A. Steiner, L. Dellantonio, R. Blatt, P. Zoller, T. Monz, P. Schindler, C. Muschik, and M. Ringbauer, *Nat. Phys.* **21**, 570 (2025).
- [7] A. Burov, J. Baglio, and C. Javerzac-Galy, (2025), [arXiv:2512.14513](https://arxiv.org/abs/2512.14513) [quant-ph].
- [8] R. Haghshenas, E. Chertkov, M. Mills, W. Kadow, S.-H. Lin, Y.-H. Chen, C. Cade, I. Niesen, T. Begušić, M. S. Rudolph, C. Cirstoiu, K. Hemery, C. M. Keever, M. Lubasch, E. Granet, C. H. Baldwin, J. P. Bartolotta, M. Bohn, J. Cline, M. DeCross, J. M. Dreiling, C. Foltz, D. Francois, J. P. Gaebler, C. N. Gilbreth, J. Gray, D. Gresh, A. Hall, A. Hankin, A. Hansen, N. Hewitt, R. B. Hutson, M. Iqbal, N. Kotibhaskar, E. Lehman, D. Lucchetti, I. S. Madjarov, K. Mayer, A. R. Milne, S. A. Moses, B. Neyenhuis, G. Park, B. Ponsioen, M. Schecter, P. E. Siegfried, D. T. Stephen, B. G. Tiemann, M. D. Urmei, J. Walker, A. C. Potter, D. Hayes, G. K.-L. Chan, F. Pollmann, M. Knap, H. Dreyer, and M. Foss-Feig, (2025), [arXiv:2503.20870](https://arxiv.org/abs/2503.20870) [quant-ph].

- [9] T. Chalopin, P. Bojović, D. Bourgund, S. Wang, T. Franz, I. Bloch, and T. Hilker, *Phys. Rev. Lett.* **134**, 053402 (2025).
- [10] R. J. MacDonell, C. E. Dickerson, C. J. T. Birch, A. Kumar, C. L. Edmunds, M. J. Biercuk, C. Hempel, and I. Kassal, *Chem. Sci.* **12**, 9794 (2021).
- [11] E. Crane, K. C. Smith, T. Tomesh, A. Eickbusch, J. M. Martyn, S. Kühn, L. Funcke, M. A. DeMarco, I. L. Chuang, N. Wiebe, A. Schuckert, and S. M. Girvin, (2024), [arXiv:2409.03747 \[quant-ph\]](https://arxiv.org/abs/2409.03747).
- [12] A. F. Kemper, A. Alvertis, M. Asaduzzaman, B. N. Bakalov, D. Baron, J. Bierman, B. Burgstahler, S. Chundury, E. R. Das, J. Furches, F. Guo, R. G. Jha, K. Klymko, A. Kushwaha, A. Li, A. Majumdar, C. O. Marrero, S. Mohapatra, C. Mori, F. Mueller, D. T. Popovici, T. Stavenger, M. Tirfe, N. M. Tubman, M. Zheng, H. Zhou, and Y. Liu, (2025), [arXiv:2511.13882 \[quant-ph\]](https://arxiv.org/abs/2511.13882).
- [13] N. P. D. Sawaya, T. Menke, T. H. Kyaw, S. Johri, A. Aspuru-Guzik, and G. G. Guerreschi, *npj Quantum Inf.* **6**, 49 (2020).
- [14] D. Saha, S. S. Iyengar, P. Richerme, J. M. Smith, and A. Sabry, *J. Chem. Theory Comput.* **17**, 6713 (2021).
- [15] A. Macridin, A. C. Y. Li, S. Mrenna, and P. Spentzouris, *Phys. Rev. A* **105**, 052405 (2022).
- [16] T. Navickas, R. J. MacDonell, C. H. Valahu, V. C. Olaya-Agudelo, F. Scuccimarra, M. J. Millican, V. G. Matsos, H. L. Nourse, A. D. Rao, M. J. Biercuk, C. Hempel, I. Kassal, and T. R. Tan, *J. Am. Chem. Soc.* **147**, 23566 (2025).
- [17] Y. Liu, S. Singh, K. C. Smith, E. Crane, J. M. Martyn, A. Eickbusch, A. Schuckert, R. D. Li, J. Sinanan-Singh, M. B. Soley, T. Tsunoda, I. L. Chuang, N. Wiebe, and S. M. Girvin, *PRX Quantum* **7**, 010201 (2026).
- [18] H. L. Nourse, V. C. Olaya-Agudelo, and I. Kassal, (2025), [arXiv:2512.20828 \[quant-ph\]](https://arxiv.org/abs/2512.20828).
- [19] J. Huh, G. G. Guerreschi, B. Peropadre, J. R. McClean, and A. Aspuru-Guzik, *Nat. Photon.* **9**, 615 (2015).
- [20] D. J. Gorman, B. Hemmerling, E. Megidish, S. A. Moeller, P. Schindler, M. Sarovar, and H. Haefner, *Phys. Rev. X* **8**, 011038 (2018).
- [21] C. Sparrow, E. Martín-López, N. Maraviglia, A. Neville, C. Harrold, J. Carolan, Y. N. Joglekar, T. Hashimoto, N. Matsuda, J. L. O'Brien, D. P. Tew, and A. Laing, *Nature* **557**, 660 (2018).
- [22] S. McArdle, S. Endo, A. Aspuru-Guzik, S. C. Benjamin, and X. Yuan, *Rev. Mod. Phys.* **92**, 015003 (2020).
- [23] C. S. Wang, J. C. Curtis, B. J. Lester, Y. Zhang, Y. Y. Gao, J. Freeze, V. S. Batista, P. H. Vaccaro, I. L. Chuang, L. Frunzio, L. Jiang, S. M. Girvin, and R. J. Schoelkopf, *Phys. Rev. X* **10**, 021060 (2020).
- [24] C. S. Wang, N. E. Frattini, B. J. Chapman, S. Puri, S. M. Girvin, M. H. Devoret, and R. J. Schoelkopf, *Phys. Rev. X* **13**, 011008 (2023).
- [25] R. J. MacDonell, T. Navickas, T. F. Wohlers-Reichel, C. H. Valahu, A. D. Rao, M. J. Millican, M. A. Currington, M. J. Biercuk, T. R. Tan, C. Hempel, and I. Kassal, *Chem. Sci.* **14**, 9439 (2023).
- [26] C. H. Valahu, V. C. Olaya-Agudelo, R. J. MacDonell, T. Navickas, A. D. Rao, M. J. Millican, J. B. Pérez-Sánchez, J. Yuen-Zhou, M. J. Biercuk, C. Hempel, T. R. Tan, and I. Kassal, *Nat. Chem.* **15**, 1503 (2023).
- [27] J. Whitlow, Z. Jia, Y. Wang, C. Fang, J. Kim, and K. R. Brown, *Nat. Chem.* **15**, 1509 (2023).
- [28] V. So, M. D. Suganthi, A. Menon, M. Zhu, R. Zhuravel, H. Pu, P. G. Wolynes, J. N. Onuchic, and G. Pagano, *Sci. Adv.* **10**, eads8011 (2024).
- [29] K. Sun, M. Kang, H. Nuomin, G. Schwartz, D. N. Beratan, K. R. Brown, and J. Kim, *Nat. Commun.* **16**, 4042 (2025).
- [30] K. H. Nielsen, Y. Wang, E. C. R. Deacon, P. I. Sund, Z. Liu, S. Scholz, A. D. Wieck, A. Ludwig, L. Midolo, A. S. Sørensen, S. Paesani, and P. Lodahl, *Nat. Commun.* **16**, 11397 (2025).
- [31] R. Gerritsma, G. Kirchmair, F. Zähringer, E. Solano, R. Blatt, and C. F. Roos, *Nature* **463**, 68 (2010).
- [32] R. Gerritsma, B. P. Lanyon, G. Kirchmair, F. Zähringer, C. Hempel, J. Casanova, J. J. García-Ripoll, E. Solano, R. Blatt, and C. F. Roos, *Phys. Rev. Lett.* **106**, 060503 (2011).
- [33] S. Saner, O. Băzăvan, D. J. Webb, G. Araneda, C. J. Ballance, R. Srinivas, D. M. Lucas, and A. Bermúdez, (2025), [arXiv:2507.19588 \[quant-ph\]](https://arxiv.org/abs/2507.19588).
- [34] Z. Davoudi, N. M. Linke, and G. Pagano, *Phys. Rev. Res.* **3**, 043072 (2021).
- [35] J. Y. Araz, M. Grau, J. Montgomery, and F. Ringer, *Phys. Rev. A* **112**, 012620 (2025).
- [36] S. A. Gardiner, J. I. Cirac, and P. Zoller, *Phys. Rev. Lett.* **79**, 4790 (1997).
- [37] C. M. Bender and T. T. Wu, *Phys. Rev.* **184**, 1231 (1969).
- [38] R. Silbey and R. W. Munn, *J. Chem. Phys.* **72**, 2763 (1980).
- [39] F. A. Miller, *Proc. Indian Acad. Sci. (Chem. Sci.)* **92**, 563 (1983).
- [40] R. W. Munn and R. Silbey, *J. Chem. Phys.* **83**, 1843 (1985).
- [41] M. Brack, R. K. Bhaduri, J. Law, and M. V. N. Murthy, *Phys. Rev. Lett.* **70**, 568 (1993).
- [42] P. Hamm and G. Stock, *Phys. Rev. Lett.* **109**, 173201 (2012).
- [43] G.-Z. Zhu, G. Lao, C. E. Dickerson, J. R. Caram, W. C. Campbell, A. N. Alexandrova, and E. R. Hudson, *J. Phys. Chem. Lett.* **15**, 590 (2024).
- [44] M. Mallweger, N. Kuk, V. Shankar, R. Thomm, H. Parke, I. Straka, W. Li, I. Lesanovsky, and M. Hennrich, (2025), [arXiv:2507.23631 \[quant-ph\]](https://arxiv.org/abs/2507.23631).
- [45] L. Faddeev and V. Korepin, *Phys. Rep.* **42**, 1 (1978).
- [46] W. C. Stewart, *Appl. Phys. Lett.* **12**, 277 (1968).
- [47] D. E. McCumber, *J. Appl. Phys.* **39**, 3113 (1968).
- [48] S. Coleman, *Phys. Rev. D* **11**, 2088 (1975).
- [49] A. C. C. de Albornoz, R. G. Cortiñas, M. Schäfer, N. E. Frattini, B. Allen, D. G. A. Cabral, P. E. Videla, P. Khazaei, E. Geva, V. S. Batista, and M. H. Devoret, (2024), [arXiv:2409.13113 \[quant-ph\]](https://arxiv.org/abs/2409.13113).
- [50] K. R. Brown, C. Ospelkaus, Y. Colombe, A. C. Wilson, D. Leibfried, and D. J. Wineland, *Nature* **471**, 196 (2011).
- [51] M. Harlander, R. Lechner, M. Brownnutt, R. Blatt, and W. Hänsel, *Nature* **471**, 200 (2011).
- [52] U. Tanaka, M. Nakamura, K. Hayasaka, A. Bautista-Salvador, C. Ospelkaus, and T. E. Mehlstäubler, *Quantum Sci. Technol.* **6**, 024010 (2021).
- [53] J. F. Niedermeyer, N. K. Lysne, K. C. McCormick, J. Keller, C. W. Hogle, M. G. Blain, E. J. Heller, R. Schmied, R. Jördens, S. L. Todaro, D. J. Wineland, A. C. Wilson, D. H. Slichter, and D. Leibfried, (2025), [arXiv:2512.08037 \[quant-ph\]](https://arxiv.org/abs/2512.08037).
- [54] D. Leibfried, B. DeMarco, V. Meyer, M. Rowe, A. Ben-Kish, J. Britton, W. M. Itano, B. Jelenković, C. Langer, T. Rosenband, and D. J. Wineland, *Phys. Rev. Lett.* **89**, 247901 (2002).
- [55] O. Băzăvan, S. Saner, D. J. Webb, E. M. Ainley, P. Drmota, D. P. Nadlinger, G. Araneda, D. M. Lucas, C. J. Ballance, and R. Srinivas, (2024), [arXiv:2403.05471 \[quant-ph\]](https://arxiv.org/abs/2403.05471).
- [56] M. Simoni, I. Rojkov, M. Mazzanti, W. Adamczyk, A. Ferk, P. Hrmo, S. Jain, T. Sägger, D. Kienzler, and

- J. Home, (2025), [arXiv:2509.05734](https://arxiv.org/abs/2509.05734) [quant-ph].
- [57] C. K. Law and J. H. Eberly, *Phys. Rev. Lett.* **76**, 1055 (1996).
- [58] M. Walschaers, *PRX Quantum* **2**, 030204 (2021).
- [59] R. T. Sutherland and R. Srinivas, *Phys. Rev. A* **104**, 032609 (2021).
- [60] V. G. Matsos, C. H. Valahu, T. Navickas, A. D. Rao, M. J. Millican, X. C. Kolesnikow, M. J. Biercuk, and T. R. Tan, *Phys. Rev. Lett.* **133**, 050602 (2024).
- [61] K. Park and R. Filip, *npj Quantum Inf.* **10**, 25 (2024).
- [62] J. Sinanan-Singh, G. L. Mintzer, I. L. Chuang, and Y. Liu, *Quantum* **8**, 1427 (2024).
- [63] Y. Liu, J. M. Martyn, J. Sinanan-Singh, K. C. Smith, S. M. Girvin, and I. L. Chuang, *IEEE Trans. Signal Process.* **73**, 3641 (2025).
- [64] J. Hong, S. H. Kim, S. K. Min, and J. Huh, (2025), [arXiv:2510.10495](https://arxiv.org/abs/2510.10495) [quant-ph].
- [65] P.-T. Fong and H.-K. Lau, (2025), [arXiv:2508.20261](https://arxiv.org/abs/2508.20261) [quant-ph].
- [66] T. Chalermputitarak, K. Schwennicke, I. Kassal, and T. R. Tan, (2025), [arXiv:2511.22286](https://arxiv.org/abs/2511.22286) [quant-ph].
- [67] T. Rainaldi, V. Ale, M. Grau, D. Kharzeev, E. Rico, F. Ringer, P. Shome, and G. Siopsis, (2025), [arXiv:2512.19582](https://arxiv.org/abs/2512.19582) [quant-ph].
- [68] L. Laneve, (2025), [arXiv:2503.03026](https://arxiv.org/abs/2503.03026) [quant-ph].
- [69] E. Shuryak, *Nucl. Phys. B* **302**, 621 (1988).
- [70] S. Coleman, *Phys. Rev. D* **15**, 2929 (1977).
- [71] R. Wild, M. Nötzold, M. Simpson, T. D. Tran, and R. Wester, *Nature* **615**, 425 (2023).
- [72] A. D. Godbeer, J. S. Al-Khalili, and P. D. Stevenson, *Phys. Chem. Chem. Phys.* **17**, 13034 (2015).
- [73] L. Slocombe, M. Sacchi, and J. Al-Khalili, *Commun. Phys.* **5**, 109 (2022).
- [74] P. H. Cribb, S. Nordholm, and N. Hush, *Chem. Phys.* **69**, 259 (1982).
- [75] F. Bouakline, *Phys. Chem. Chem. Phys.* **23**, 20509 (2021).
- [76] H. V. L. Nguyen, I. Gulaczyk, M. Kreglewski, and I. Kleiner, *Coord. Chem. Rev.* **436**, 213797 (2021).
- [77] D. Mitoli, M. Petrov, J. Maul, W. B. Stoll, M. T. Ruggerio, and A. Erba, *J. Chem. Theory Comput.* **21**, 5365 (2025).
- [78] H. V. L. Nguyen, *J. Phys. Chem. Lett.* **16**, 104 (2025).
- [79] H. F. Trotter, *Proc. Am. Math. Soc.* **10**, 545 (1959).
- [80] V. G. Matsos, C. H. Valahu, M. J. Millican, T. Navickas, X. C. Kolesnikow, M. J. Biercuk, and T. R. Tan, *Nat. Phys.* **21**, 1664 (2025).
- [81] J. P. Home, D. Hanneke, J. D. Jost, D. Leibfried, and D. J. Wineland, *New J. Phys.* **13**, 073026 (2011).
- [82] T. R. Tan, T. Navickas, C. Valahu, J. Jee, A. Rao, M. Millican, and M. Biercuk, in *Joint Conference of the European Frequency and Time Forum and IEEE International Frequency Control Symposium (EFTF/IFCS)* (2023) pp. 1–2.
- [83] C. Flühmann and J. P. Home, *Phys. Rev. Lett.* **125**, 043602 (2020).
- [84] C. Gerry and P. Knight, *Introductory Quantum Optics*, 1st ed. (Cambridge University Press, 2004) p. 65.
- [85] M. Shapiro and P. Brumer, *Quantum Control of Molecular Processes* (John Wiley & Sons, 2011).
- [86] D. Kiesenhofer, H. Hainzer, A. Zhdanov, P. C. Holz, M. Bock, T. Ollikainen, and C. F. Roos, *PRX Quantum* **4**, 020317 (2023).
- [87] G. A. Worth, H.-D. Meyer, H. Köppel, L. S. Cederbaum, and I. Burghardt, *Int. Rev. Phys. Chem.* **27**, 569 (2008).
- [88] V. C. Olaya-Agudelo, B. Stewart, C. H. Valahu, R. J. MacDonell, M. J. Millican, V. G. Matsos, F. Scuccimarra, T. R. Tan, and I. Kassal, *Phys. Rev. Res.* **7**, 023215 (2025).
- [89] I. R. Craig, M. Thoss, and H. Wang, *J. Chem. Phys.* **127**, 144503 (2007).
- [90] A. Van Haeften, C. Ash, and G. Worth, *J. Chem. Phys.* **159**, 194114 (2023).
- [91] C. Guo, M. Mukherjee, and D. Poletti, *Phys. Rev. A* **92**, 023637 (2015).
- [92] T. Chen, V. Balachandran, C. Guo, and D. Poletti, *Phys. Rev. E* **102**, 012155 (2020).
- [93] S. Gao, *Phys. Rev. B* **57**, 4509 (1998).
- [94] S. Gao, J. Strömquist, and B. I. Lundqvist, *Phys. Rev. Lett.* **86**, 1805 (2001).
- [95] C. McGarry, T. Chalermputitarak, K. Schwennicke, F. Scuccimarra, M. J. Millican, V. G. Matsos, C. H. Valahu, H.-K. Chan, H. L. Nourse, I. Kassal, and T. R. Tan, *Zenodo dataset*, 10.5281/zenodo.18752287 (2026).
- [96] D. Leibfried, R. Blatt, C. Monroe, and D. Wineland, *Rev. Mod. Phys.* **75**, 281 (2003).
- [97] C. Monroe, D. M. Meekhof, B. E. King, S. R. Jefferts, W. M. Itano, D. J. Wineland, and P. Gould, *Phys. Rev. Lett.* **75**, 4011 (1995).